Docking Strategy for a Space Station Container Docking Device Based on Adaptive Sensing

GANG WANG[1], **ZHIJIE XIE**[1], **XINGKE MU**[2], **SHAOZHEN LI**[1], **FEI YANG**[1],
HONGHAO YUE[1], **AND SHENGYUAN JIANG**[1]

[1]School of Mechatronics Engineering, Harbin Institute of Technology, Harbin 150080, China
[2]China Academy of Launch Vehicle Technology Research and Development, Beijing 100076, China

Corresponding author: Fei Yang (yf2003420@163.com)

ABSTRACT A fractional-step docking strategy based on adaptive sensing is proposed for an orthogonally distributed container docking device that exhibits various characteristics, including modularization, miniaturization, extensibility, and peripheral layout. A dynamic model of a body combined with a space station container and robotic arm and a contact dynamic model between the combined body and the docking device are established to lay the foundation for the docking determination of the container in limit poses. Taking the structural and dynamic characteristics of the orthogonally distributed docking device into consideration, the actions of a diagonal double-docking hook were matched under limited working conditions. A 6-D force sensor placed at the end of the robotic arm was used to perceive the contact force of the container and the position of the docking hook, providing a basis for selecting a docking strategy. The tolerance of the docking device was analyzed when applying the docking strategy, the results of which demonstrated a much larger tolerance than that found in the synchronous docking. An orthogonally distributed docking device and an experimental platform were developed, and the tolerance of the device when using the adaptive sensing docking strategy was tested and verified. A comparison between the experiment and simulation proves the effectiveness and feasibility of the proposed adaptive sensing docking strategy.

INDEX TERMS Orthogonally distributed, docking device, adaptive sensing, fractional-step docking strategy.

I. INTRODUCTION

Docking technology for an on-orbit cooperative target exhibits broad application prospects in tasks including space station container docking, on-orbit services, and module docking [1]–[4]. Given the rapid development in commercial space travel, reusable low-cost docking devices have become a popular research topic. Modularization, miniaturization, and scalability are new requirements for docking devices. The level of tolerance determines the success or failure of container docking missions, and is also an important indicator of the performance of a docking device. A few previous studies have examined several schematic and docking dynamics on traditional docking devices, and a few ground tests and on-orbit demonstrations have been conducted [5]–[8]. To achieve reliable locking of the container during the launch phase and orbit, and a second docking and locking of the returning supplies upon return to the ground,

Japan's H-II Transfer Vehicle (HTV) places a repeat HTV cargo attachment mechanism between the container and pallet, which can resist the acceleration impact caused by vibrations during launch and a change in orbit [9]. In 2009, the U.S. launched the space shuttle Endeavour to carry the test tools and platforms required by astronauts to work on the International Space Station (ISS). The repeated docking and separation device applied between a container and space shuttle realized an accurate connection through a jaw and v-groove, and a repeated docking lock of the container was finally realized [10]. In 2007, the United States launched the Orbital Express spacecraft with the aim of validating on-orbit service technology [11]. With the assistance of a space manipulator, a target spacecraft was docked by the tracking spacecraft through an interlocking triangular cross-docking mechanism to provide space support for on-orbit services [12], [13]. In [14], Orbital Recovery Corporation initiated the SMART-OLEV system in 2007 to dock a target spacecraft using a "cone-rod" docking mechanism and provided services including propulsion, navigation, control, maintenance, and

The associate editor coordinating the review of this manuscript and approving it for publication was Ning Sun.

fueling. Furthermore, the use of a Shuttle Remote Manipulator System (SRMS) and the Japanese Experimental Module, Remote Manipulator System (JEMRMS) on the International Space Station have also been discussed [15], [16]. Docking devices are unsuitable for reusable docking of containers given the large-size wire rope used to tighten the docking rod. China, the United States, and the former Soviet Union conducted multiple cabin docking missions using a cone-rod docking device and an Allomorphic peripheral docking device in [17]–[19]. Aiming at an SRMS end-effector, Akira Tsuchihashi completed the design of a torque sensor and a positioning sensor based on a micro-stroke switch, and proposed a terminal effector docking operation strategy [20]. Jiegao Wang conducted a contact dynamics simulation of an SRMS end-effector for a robotic arm docking operation used in the maintenance of the Hubble space telescope and a derailment service robot system, and proposed an on-orbit autonomous docking strategy for a robotic system [21], [22]. Yisong Tan developed a set of devices made up of a large robotic arm end-effector for the space station, and proposed the docking strategy of a loop/contact transport module [23]. Fei Feng studied the docking strategy of the end-effector according to the results of the identification of the parameters of the on-orbit container for the mixed inertia of the target mass and the positional relationship between the docking rod and end-effector [24]. According to the dynamic parameters and a deviation of the container, different docking strategies were selected to improve the efficiency and smoothness of the docking performance. According to the measurement results of the docking device sensor, Yu Zhang adopted a force control strategy, speed strategy, and blind exploration docking strategy to enhance the docking capability of the target aircraft nozzle and improve the docking success rate [25]. Some scholars improve the performance of equipment by introducing neural network and optimal control. A neural network-based adaptive control method can provide effective control for both actuated and unactuated state variables based on the original nonlinear ship-mounted crane dynamics without any linearizing operations [26]. An energy-optimal solution for transportation control of double pendulum cranes is proposed [27]. By applying the presented approach, the transportation objective, including fast trolley positioning and swing elimination, is achieved with minimized energy consumption.

The device used in docking and robotic arm docking missions has applied a cone-rod, an allogeneic isomorphic perimeter, wire rope folding, and a three-finger docking mechanism. Research into docking strategies considers all these types of symmetrical centralized docking devices to control the overall docking speed, contact damping, and docking torque as a whole. When compared with a traditional central symmetric centralized docking device, the orthogonally distributed docking device is more complicated in terms of the structural layout, and hence it is more difficult to devise a docking strategy for it. At present, no studies on docking strategies suitable for such devices have been found in the public literature. This paper proposes an adaptive sensing docking strategy for orthogonally distributed docking devices, which effectively improves the tolerance. The contributions of this paper are as follows: (1) The adaptive docking strategy for orthogonal distributed container docking device is proposed. (2) The dynamic model of orthogonal distributed docking device is established, and the tolerance of adaptive docking strategy is determined by simulation analysis. (3) The prototype of orthogonal distributed docking device was developed and a docking test platform was built. The experimental verification of the proposed adaptive docking strategy is carried out. The advantage of using fractional-step adaptive docking strategy is that the tolerance capacity of docking devices has been significantly improved compared with that of using synchronous docking strategy.

The remainder of this study is divided into the following six sections: Section I introduces the different types of traditional docking devices and the docking strategy. Section II introduces the orthogonally distributed docking device and describes the tolerance capability analysis method applied. The proposed docking strategy based on adaptive sensing is and elaborated upon in Section III. Section IV analyzes the tolerance capacity of the docking device when using the docking strategy. Section V describes the experimental platform established to test and verify the tolerance capability under the adaptive sensing docking strategy. Finally, Section VI summarizes the advantages of the adaptive sensing docking strategy.

II. ORTHOGONALLY DISTRIBUTED DOCKING DEVICE AND ITS TOLERANCE ANALYSIS METHOD
A. ORTHOGONALLY DISTRIBUTED DOCKING DEVICE AND ITS WORKING PROCESS

Space stations are used by astronauts for long periods of time, to carry out a large number of scientific research experiments. During the operation and maintenance of a space station, the living materials and experimental equipment of the astronauts need to be continuously supplemented, updated, and maintained. A specific implementation plan of a replacement mission for space station materials is as follows: (1) The materials and equipment needed for the space station are loaded into the exposed facility (EF) payload container. The EF payload container is then locked onto the experiment logistics module-exposed section (ELM-ES) through the docking device, and the ELM-ES is carried in the cargo bay of the space shuttle. (2) The shuttle carrying the ELM-ES launches into a predetermined orbit and docks with the ISS. (3) The EF payload containers in the ELM-ES of the space shuttle and the EF payload containers on the exposed equipment platform of the ISS are swapped using a robotic arm and the docking device, completing the replacement of the supplies and equipment of the ISS. (4) The shuttle then returns to the ground with the ELM-ES and the replaced EF payload containers, and the failed equipment in the container can be repaired, as shown in Fig. 1.
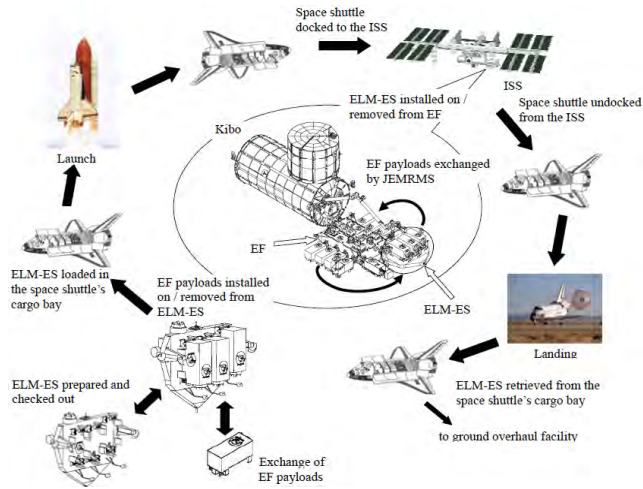
FIGURE 1. EF payloads container replacement in the ISS.

(a) Before docking device operation
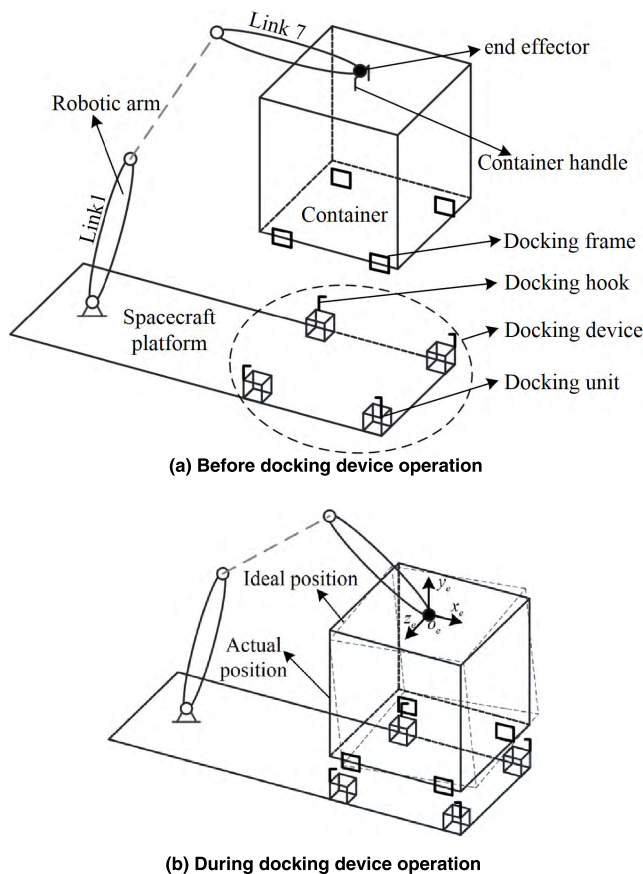

(b) During docking device operation

FIGURE 2. Structure of the docking device.

The main function of the docking device involves completing a pose adjustment and the docking and locking of the container with the assistance of a robotic arm. Both the robotic arm and the docking device are fixed to the operational platform of the space station, as shown in Fig. 2(a). Prior to the operation of the docking device, the end effector of the robotic arm locks the container handle to form a unitary body and carries the container to the docking area of the device. Given the

joint error and deformation of the robotic arm, a certain pose deviation of the container exists relative to the ideal docking position, as shown in Fig. 2(b). If the pose deviation e of the container corresponds to (Δx, Δy, Δz, $\Delta\alpha$, $\Delta\beta$, $\Delta\gamma$), then the actual pose of the container is translated as Δx, Δy, Δz relative to the ideal pose along the x_e, y_e, and z_e axes, and is rotated as $\Delta\alpha$, $\Delta\beta$, $\Delta\gamma$ around the x_e, y_e, and z_e axes, respectively, at the end coordinate system of the robotic arm.

During the operation of the docking device, the joint of the robotic arm is affected only by the viscous damping associated with the joint speed and not the motor drive torque. This state is termed a zero-force control state. In the control state, the robotic arm can move if the force at the end of the robotic arm is more than F_{e0}. The docking device is composed of four docking units U_a, U_b, U_c, and U_d. The docking unit uses a hook-frame structure as the docking execution component, as shown in Fig. 3. The docking hook moves at a certain speed on the docking unit, and the docking frame is fixed at the bottom of the container. The direction of the two adjacent docking hooks is orthogonal, and this layout allows for more reliable docking of the containers. The docking hooks in the four docking units U_a, U_b, U_c, and U_d are called H_a, H_b, H_c, and H_d, and the docking frames are called F_a, F_b, F_c, and F_d.
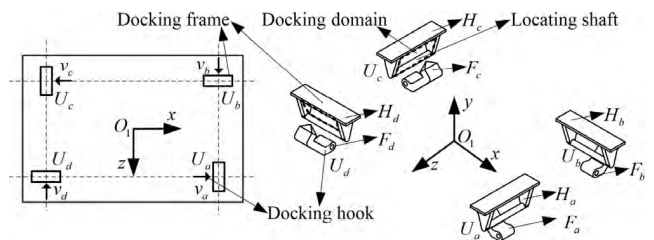

FIGURE 3. Docking component layout.

B. TOLERANCE CAPABILITY ANALYSIS METHOD

The docking tolerance refers to the ability to allow pose errors at the handle of the container while ensuring reliable docking. The larger the allowable error is, the larger the tolerance of the docking device will be. In the case of synchronous docking of the docking hook, the tolerance capacity of the docking device is known to be $T_0 = [\pm 10mm, \pm 10\ mm, \pm 10\ mm, \pm 1°, \pm 1°, \pm 1°]$. According to the working characteristics of the orthogonal distributed docking device, a tolerance capacity analysis method is proposed, as shown in Fig. 4, the key steps of which are as follows:

(1) The synchronous docking tolerance is T_0, the adaptive docking tolerance is $T = T_0 + n\Delta T$, and the initial value of n is 1.

(2) The tolerance capacity T is converted into k types of limit poses that can be validated.

(3) The k types of limit poses are simplified into j types.

(4) The changes in the container pose for j limit poses during the docking process are predicted, and it is determined whether the docking is successful. If all dockings are
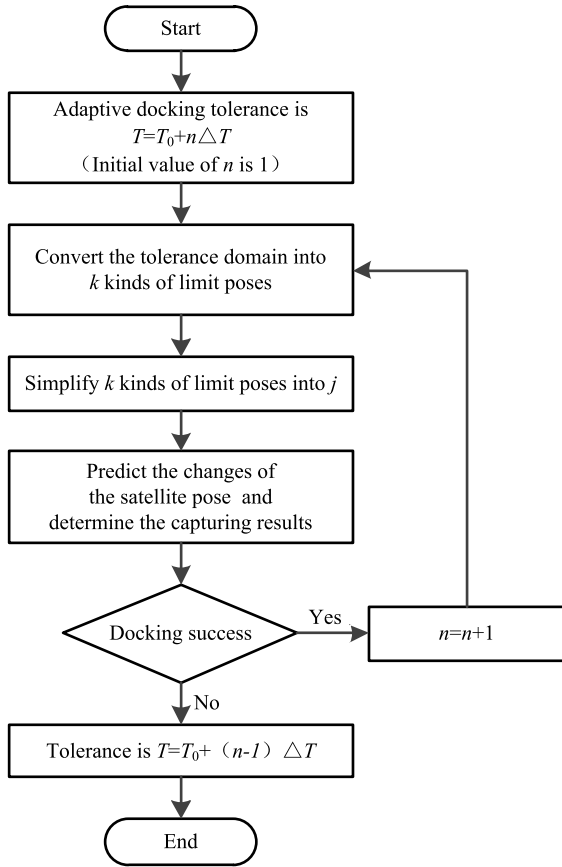
FIGURE 4. Flow chart of the tolerance analysis method.

successful, the tolerance capacity of the device becomes greater than or equal to the tolerance T. If $n = n+1$, proceed to step (1). If not all docking procedures are successful, the tolerance of the docking device is $T = T_0 + (n-1)\Delta T$.

1) TOLERANCE DOMAIN TRANSFORMATION AND CLASSIFICATION

The ability of the tip of the docking hook to pass through the docking frame is used as the basis to determine a reliable docking. The larger the pose error at the handle of the container, the greater the distance from the actual position to the ideal position of the docking frame, and the smaller the docking domain through which the docking hook tip can pass. If the tolerance domain corresponds to $T_m = [\pm x_m, \pm y_m, \pm z_m, \pm \alpha_m, \pm \beta_m, \pm \gamma_m]$, the docking device can then dock the container when the pose error e at the container handle is within the range specified in (1) as follows:

$$\begin{cases} -x_m \leq \Delta x \leq x_m, -y_m \leq \Delta y \leq y_m, -z_m \leq \Delta z \leq z_m, \\ -\alpha_m \leq \Delta \alpha \leq \alpha_m, -\beta_m \leq \Delta \beta \leq \beta_m, -\gamma_m \leq \Delta \gamma \leq \gamma_m \end{cases}$$
$$(1)$$

The limit error e_{li} can be obtained by taking the maximum or minimum value of each parameter of pose error e within the tolerance domain T_m. Because the limit error e_{li} contains six parameters, a total of $K = 2^6 = 64$ different

limit errors e_{li} can be obtained. The limit pose of the container corresponding to each type of limit error e_{li} corresponds to limit pose p_{eli}. If each parameter of e_{l1} is the maximum within the value range, it can be expressed as follows:

$$e_{l1} = [x_m, y_m, z_m, \alpha_m, \beta_m, \gamma_m].$$
$$(2)$$

where E_L denotes the set of limit error e_{li}, and the corresponding limit pose set of the container is P_{EL}. Specifically, E_L is expressed as follows:

$$E_L = [e_{l1}, \cdots e_{li}, \cdots e_{l64}] \quad (i = 1, 2, \cdots 64).$$
$$(3)$$

Evidently, if the container is docked under the condition of all 64 limit errors e_{li}, it proves that the container is docked within the tolerance domain T_m. Thus, the tolerance domain of the docking device is determined by checking the docking result of the limit pose p_{eli} corresponding to the limit error e_{li}.

If all limit poses corresponding to the 64 limit errors have to be validated, the analysis is extremely complicated. Instead, the 64 limit poses are classified into four types based on the contacting order of the four docking unit components. Given the symmetrical structural characteristics of the orthogonally distributed docking device, one type of limit pose is selected to represent all limit poses. The pose prediction and docking determination during the docking process of the selected type of limit pose are used as the basis for tolerance determination.

2) ROBOTIC ARM-CONTAINER COMBINED BODY CONTACT DYNAMICS MODEL

Before the docking process starts, the robotic arm carries the container and stabilizes it for a period of time, making the container and the docking device relatively static. During the docking process, the docking component moves slowly and the contact force is small. Since the mass of the aircraft is much larger than that of the container, the influence of small contact force on the pose of the spacecraft can be ignored. So we can treat the spacecraft platform as a fixed base, and just analyze the movement of the target container relative to the docking device.

The robotic arm in the study exhibits seven degrees of freedom and consists of seven links. The motion of the robotic arm-container combined body is determined via its dynamic characteristics. Thus, the dynamics analysis of the combined body corresponds to the basis for the pose prediction and control strategy. A simplified dynamics model of the combined body was constructed to analyze the dynamic properties of the combined body. The end effector and the container are consolidated into a rigid body, and thus the kinematic model of the combined body is identical to that of the robotic arm as shown in Fig. 5. The centroid and moment of inertia of the last link varies in the dynamic model of the combined body when compared with the dynamic model of the robotic arm [28].
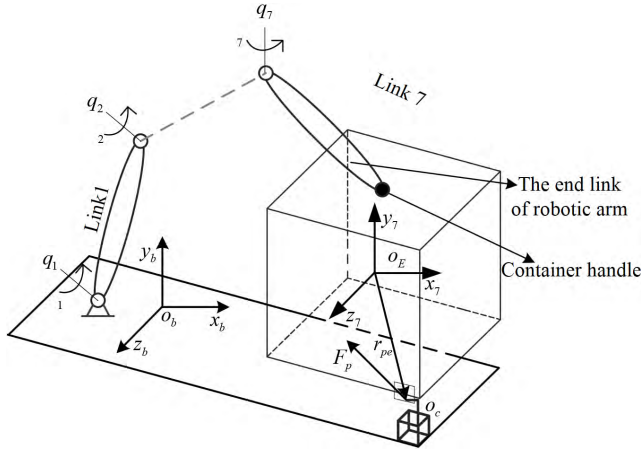
FIGURE 5. Model of the robotic arm-container combined body.

The coordinate transformation of the robotic arm links is expressed as follows:

$$
{}^{i}A_{i+1} = \begin{bmatrix} c\theta_i & -s\theta_i c\alpha_i & s\theta_i s\alpha_i & a_i c\theta_i \\ s\theta_i & c\theta_i c\alpha_i & -c\theta_i s\alpha_i & a_i s\theta_i \\ 0 & s\alpha_i & c\alpha_i & d_i \\ 0 & 0 & 0 & 1 \end{bmatrix} \tag{4}
$$

The transformation matrix from the base of the robotic arm to any link is as follows:

$$
T_i = {}^{0}A_1 \cdots {}^{i-1}A_i \tag{5}
$$

We consider the robotic arm-container combined body as the analysis object, and the Lagrange second equation is used to establish the dynamic model. We define the Lagrangian function as L, E denotes the kinetic energy of the system, V denotes the potential energy of the system, and Ψ denotes the energy loss of the system. The Lagrangian equation is expressed as follows:

$$
\begin{cases} \dfrac{d}{dt}\left(\dfrac{\partial L}{\partial \dot{q}}\right) - \dfrac{\partial L}{\partial q} + \dfrac{\partial \psi}{\partial \dot{q}} = Q \\ L = E - V \end{cases} \tag{6}
$$

where Q denotes the generalized force matrix, and q denotes the generalized coordinates of joint.

The generalized coordinates are selected as follows:

$$
q = [\theta_1 \quad \theta_2 \quad \theta_3 \quad \theta_4 \quad \theta_5 \quad \theta_6 \quad \theta_7]^{\mathrm{T}} \tag{7}
$$

With respect to each generalized coordinate, the generalized force is defined as follows:

$$
Q = [\tau_1 \quad \tau_2 \quad \tau_3 \quad \tau_4 \quad \tau_5 \quad \tau_6 \quad \tau_7]^{\mathrm{T}} \tag{8}
$$

The position vector of a particle in the global coordinate system is obtained from the position vector of a particle in the body-fixed coordinate system:

$$
r_i = {}^{0}T_i \, {}^{i}r \tag{9}
$$

where ${}^{i}r$ denotes the position vector of a particle in body-fixed coordinate system, and r_i denotes the position vector of a particle in the global coordinate system.

The position vector of a particle on the ith link on the robotic arm in the global coordinate system is given by generalized coordinates as follows:

$$
r_i = r_i(q_1, q_2, q_3, q_4, q_5, q_6, q_7) \tag{10}
$$

The homogeneous velocity of the particle is defined as follows:

$$
\dot{r}_i = {}^{0}\dot{T}_i \, {}^{i}r = \left(\sum_{j=1}^{i} \frac{\partial {}^{0}T_i}{\partial q_j} \dot{q}_j \right) {}^{i}r \tag{11}
$$

Therefore, the kinetic energy of the particle is as follows:

$$
\begin{aligned}
dE_i &= \frac{1}{2}\dot{r}_i \cdot \dot{r}_i dm = \frac{1}{2} diag(\dot{r}_i \dot{r}_i^{\mathrm{T}}) dm \\
&= \frac{1}{2} diag\left[\sum_{j=1}^{i}\sum_{k=1}^{i} \frac{\partial {}^{0}T_i}{\partial q_j} {}^{i}r \, {}^{i}r^{\mathrm{T}} \frac{\partial ({}^{0}T_i)^{\mathrm{T}}}{\partial q_k} \dot{q}_j \dot{q}_k \right] dm
\end{aligned} \tag{12}
$$

Thus, the kinetic energy of the link i is as follows:

$$
\begin{aligned}
E_i &= \int_i dE_i = \frac{1}{2}\int_i diag\left[\sum_{j=1}^{i}\sum_{k=1}^{i} \frac{\partial {}^{0}T_i}{\partial q_j} {}^{i}r \, {}^{i}r^{\mathrm{T}} \frac{\partial ({}^{0}T_i)^{\mathrm{T}}}{\partial q_k} \dot{q}_j \dot{q}_k \right] dm \\
&= \frac{1}{2} diag\left\{ \sum_{j=1}^{i}\sum_{k=1}^{i} \frac{\partial {}^{0}T_i}{\partial q_j} J_i \frac{\partial ({}^{0}T_i)^{\mathrm{T}}}{\partial q_k} \dot{q}_j \dot{q}_k \right\}
\end{aligned} \tag{13}
$$

where J_i denotes a symmetric constant matrix that completely describes the mass distribution of the link i.

The kinetic energy of the combined body includes the kinetic energy of each link and that of the container. The seventh link of the robotic arm and the container constitutes a rigid body, and the kinetic energy of the container is contained in the seventh link. The kinetic energy of the combined body is expressed as follows:

$$
\begin{aligned}
E_i &= \sum_{i=1}^{7} E_i \\
&= \frac{1}{2} \sum_{i=1}^{6}\sum_{j=1}^{i}\sum_{k=1}^{i} diag\left(\frac{\partial {}^{0}T_i}{\partial q_j} J_i \frac{\partial ({}^{0}T_i)^{\mathrm{T}}}{\partial q_k} \right) \dot{q}_j \dot{q}_k \\
&= \frac{1}{2}\dot{q}^{\mathrm{T}} D(q)\dot{q}
\end{aligned} \tag{14}
$$

where $D(q)$ denotes the inertia matrix of the robotic arm.

The robotic arm-container combined body works in space in a microgravity environment. We ignore the change in potential energy of the combined body, and thus $V = 0$. The kinetic energy is inserted into the Lagrangian function, and the partial derivatives of the generalized coordinates are calculated as follows:

$$
\frac{\partial L}{\partial \dot{q}_j} = \frac{\partial E}{\partial \dot{q}_j} = \sum_{k=1}^{7} d_{ij}\dot{q}_k \tag{15}
$$

$$\frac{d}{dt}\frac{\partial L}{\partial \dot{q}_j} = \frac{\partial E}{\partial \dot{q}_j} = \sum_{k=1}^{7} d_{ij}\ddot{q}_k + \sum_{k=1}^{7} \dot{d}_{ij}\dot{q}_k \qquad (16)$$

$$\frac{\partial L}{\partial q_j} = \frac{\partial E}{\partial q_j} = \frac{1}{2}\dot{q}^{\mathrm{T}}\frac{\partial \boldsymbol{D}}{\partial q_j}\dot{q} \qquad (17)$$

The energy loss of each joint of the robotic arm is expressed as follows:

$$\psi = \sum_{i=1}^{7} \psi_i = \frac{1}{2}\sum_{i=1}^{7} f_i\dot{q}_i^2 \qquad (18)$$

$$\frac{\partial \psi}{\partial \dot{q}} = \sum_{i=1}^{7} f_i\dot{q}_i \qquad (19)$$

where f_i denotes the viscous damping coefficient of the ith joint.

We substitute equations (15), (16), (17), and (19) into the Lagrangian equation as follows:

$$\sum_{k=1}^{7} d_{jk}\ddot{q}_k + \sum_{k=1}^{7} \dot{d}_{jk}\dot{q}_k - \frac{1}{2}\dot{q}^T\frac{\partial \boldsymbol{D}}{\partial q_j}\dot{q} + \sum_{j=1}^{7} f_j\dot{q}_j$$
$$= \tau_j \quad j = 1, \cdots, n \qquad (20)$$

This is also simplified as follows:

$$D\ddot{q} + H\dot{q} + f\dot{q} = \tau \qquad (21)$$

where $\boldsymbol{D}$ denotes the system positive definite inertia matrix. Additionally, $\boldsymbol{H}$ denotes the coefficient matrix containing Coriolis force and centrifugal force, and $\boldsymbol{f}$ denotes the viscous damping matrix.

We substitute $\boldsymbol{F_p}$ into the Lagrange equation as follows:

$$D\ddot{q} + H\dot{q} + f\dot{q} = J_p F_p \qquad (22)$$

where $\boldsymbol{J_p}$ denotes the motion Jacobian matrix associated with contact points.

The pose trajectory of the container is predicted from the initial conditions and equation (22). If the docking frame is always in the docking domain of the docking hook, then it is determined that the docking is successful. Conversely, the docking fails if the docking frame escapes the docking domain of the docking hook.

III. FRACTIONAL-STEP ADAPTIVE DOCKING STRATEGY

Repeated docking devices and robotic arms are required to operate for an extended period while in orbit. A robotic arm repeatedly carries out docking tasks in a harsh space environment, and the target container having a relative speed to the robotic arm will make the robotic arm bear the impact force. Long-term impact forces deform the robotic arm joint and arm, thereby reducing the control precision. The dimensional accuracy from the handle to the docking frame reduces in the harsh environment of alternating heat and cold in space when the target container is operated in orbit for a prolonged period. In these cases, the tolerance of the original docking device is unable to meet the higher level of tolerance required by the docking task. In the case of a fixed structure and size of the

docking device, an adaptive docking strategy is proposed to improve the device tolerance.

A. FRACTIONAL-STEP DOCKING STRATEGY

A matching strategy for four docking hooks applied during the docking process was studied in order to improve the tolerance. Based on the system perception information, the specific docking parameters of the four docking hooks were developed, including the docking speed, docking sequence, and starting time.

1) DIAGONAL DOUBLE DOCKING HOOK ACTION MATCHING

The four docking units of the docking device are orthogonal in the distribution. In one group, two docking hooks H_b and H_d along the diagonal are matched face to face, and in the other group, H_a and H_c along the diagonal are matched back to back to complete the docking operation, as shown in Fig. 3. Therefore, research on the matching of two docking hooks along each diagonal is the basis of the research on the docking strategy of the docking device. Two face-to-face docking hooks, H_b and H_d, were taken as examples for research, and the positional relationship is as shown in Fig. 6.
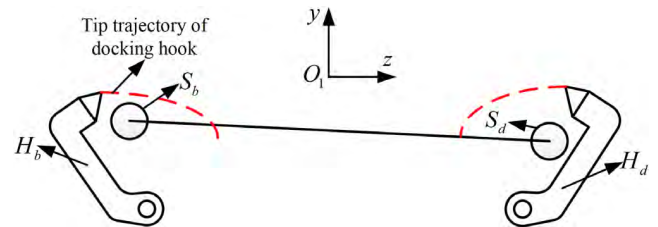

FIGURE 6. Positional relation of two face-to-face docking hooks.

Considering the overall structural characteristics of the docking device, it was found that the movement of the docking frame at the bottom of the container in the directions of the x axis and z axis was limited by the four docking hooks, and the movement in the direction of the $-y$ axis was limited by the base of the docking unit, and thus the escape direction was only in the direction of the $+y$ axis. Aiming at the escape direction of the docking frame, the docking strategy and tolerance enhancement were studied.

Analysis is performed using an example of a docking frame that escapes from the docking hook during the docking process, as indicated in Fig. 7. The positioning shaft S_b is located below the vertex trajectory of the docking hook H_b. In the docking process, one of the docking hooks H_d always makes contact with the positioning shaft S_d first and forces the container to move slowly under the contact force f_d. The other positioning shaft S_b produces postural changes owing to the overall movement of the container. When the input parameters of the model, such as the container posture are determined, the motion trajectory of the positioning shaft S_b can be solved using the contact dynamics model proposed in section II. However, when the robotic arm has errors and
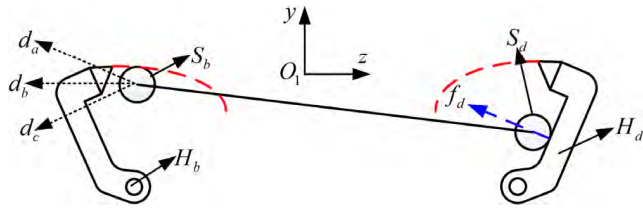
FIGURE 7. Movement direction of the docking component.

does not carry a camera, the initial conditions for the calculation of the dynamic model cannot be determined, and thus the contact dynamic model cannot be used for a trajectory prediction or docking judgment.

In the absence of a basis for judgment, a sub-case discussion was conducted. The movement direction of the positioning shaft S_b can be divided into three cases, as shown in Fig. 7. The direction of d_b is along the direction of the $-z$ axis, namely, the horizontal direction. The direction of d_a is between the $-z$ axis direction and the $+y$ axis direction, and the direction of d_c is between the $-z$ axis direction and the $-y$ axis direction. When the positioning shaft S_b moves in the direction of d_b and d_c, as the docking continues, the docking hook H_b will gradually restrict the positioning shaft S_b to move in the escape direction (the $+y$ axis direction), and finally the docking is successful. When the positioning shaft S_b moves in the d_a direction, the positioning shaft S_b may escape from the docking domain of the docking hook H_c and move in the escape direction (the $+y$ axis direction), eventually leading to a docking failure.
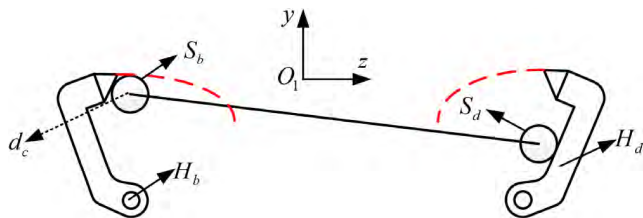

FIGURE 8. Movement direction of the docking component.

A step-by-step matching docking strategy for a diagonal double docking hook is proposed targeting the situation leading to a docking failure. Before the docking hook H_d pushes the positioning shaft S_d, the docking hook H_b is made to move into contact with the positioning shaft S_b, as shown in Fig. 8. Then, under the condition that the docking hook H_b prevents the positioning shaft S_b from moving in the escape direction, the docking hooks H_d and H_b jointly carry out the docking action, greatly improving the reliability of the docking.

2) FRACTIONAL-STEP DOCKING STRATEGY OF FOUR DOCKING HOOKS

The docking device consists of two pairs of diagonal docking units, each of which adopts the docking strategy proposed in section III A1. By considering the coordination problem of four docking units comprehensively, the docking strategy of

the entire device is obtained. Let X_{ha}, X_{hb}, X_{hc}, and X_{hd} be the displacement of the four docking hooks H_a, H_b, H_c, and H_d, respectively. When the positioning shaft S_a first contacts the docking hook H_a in the docking unit U_a, the numerical value of the displacement X_{ha} is x_{ca}. Similarly, x_{cb}, x_{cc}, and x_{cd} are the displacement values of X_{hb}, X_{hc}, and X_{hd}, when the corresponding docking components in U_b, U_c, and U_d make first contact. The total displacement of each docking hook is the same, namely, x_c.

During the process of adaptive sensing, the slider drives the four docking hooks uniformly at the same speed. The hooks H_a, H_b, H_c, and H_d were closed in order, and stopped when the docking hook and docking frame were in contact. Considering that there may be no contact between a docking hook and the corresponding docking frame in the whole movement track, in the adaptive sensing stage, if the docking hook moves to the displacement x_{cl} and still does not touch, the docking hook will stop in the displacement x_{cl}. In the adaptive docking stage, the four docking hooks are closed simultaneously according to the speed shown in Tab. 1, and moved simultaneously until docking is achieved. The adoption of this docking strategy can ensure that both pairs of docking hooks match according to the diagonal docking hook matching strategy proposed in section III A1 and improve the docking tolerance and reliability.

TABLE 1. Fractional-step docking time and travel of docking hook.

NO.	Time required	Travel	Speed	Moving docking hook	Controller
1	t_{ca}	x_{ca}	v	a	Sensing the contact position of a docking hook, the minimum travel of a docking hook is x_{cr}
2	t_{cb}	x_{cb}	v	b	
3	t_{cc}	x_{cc}	v	c	
4	t_{cd}	x_{cd}	v	d	
5	$t_{cr}=x_{cr}/v$	$x_c - x_{ca}$	$(x_c - x_{ca})/t_{cr}$	a	Adaptive docking
		$x_c - x_{cb}$	$(x_c - x_{cb})/t_{cr}$	b	
		$x_c - x_{cc}$	$(x_c - x_{cc})/t_{cr}$	c	
		$x_c - x_{cd}$	$(x_c - x_{cd})/t_{cr}$	d	

B. ADAPTIVE SENSING

Adaptive sensing is an important aspect of the fractional-step docking strategy. The meaning of adaptive sensing is: in the case of uncertain position and posture of the container, four docking hooks are respectively controlled to contact the corresponding docking frame. The position of four docking hooks in contact with the corresponding docking frame is sensed by a six-dimensional force sensor, which could be used as the basis for the selection of docking strategy.

The specific implementation method of adaptive sensing is: in the case of uncertain position and posture of the container, docking hook H_a starts docking first. When docking hook H_a contacts docking frame F_a, the six-dimensional force sensor will sense the contact force, and the controller will stop docking hook H_a after receiving the force signal. The position of docking hook H_a at this time is recorded. Similarly, the positions of the other three docking hooks and corresponding docking frames when they first contact are recorded. Therefore, when each docking hook moves independently, the first contact time t_{ca}, t_{cb}, t_{cc}, and t_{cd} with the docking frame can be obtained. In this way, the displacements x_{ca}, x_{cb}, x_{cc}, and x_{cd} and their order based on size can be calculated to provide a basis for the selection of docking strategies. The workflow of the system is shown in Fig. 9.
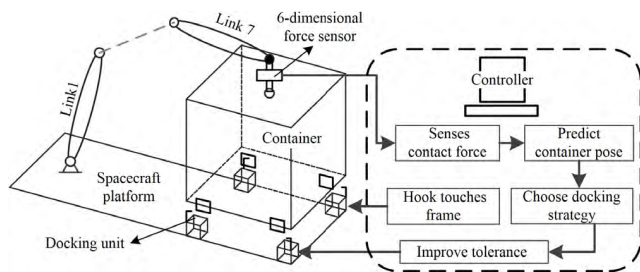

FIGURE 9. Flow chart of adaptive fractional-step docking strategy.

IV. TOLERANCE CAPABILITY ANALYSIS

To verify the correctness of the proposed contact dynamics model and the effectiveness of the docking strategy, a dynamic model was established to simulate the robotic arm, the container, and the docking device. The proposed docking strategy targets docking devices with orthogonal distribution characteristics, which have modularity and expansibility. During specific tasks, docking devices can be expanded and contracted according to the actual size of the container. To verify and test the mathematical model, the dimensions of the simulated robotic arm, container, and docking device are appropriately reduced. The system model is shown in Fig. 10.

D-H parameters of the robotic arm are shown in Tab. 2.

TABLE 2. D-H parameters of the robotic arm.

Link	θ	d	a	α
1	θ_1	0	0	$\pi/2$
2	θ_2	400	0	$\pi/2$
3	θ_3	0	0	$\pi/2$
4	θ_4	400	0	$\pi/2$
5	θ_5	0	0	$\pi/2$
6	θ_6	400	0	$\pi/2$
7	θ_7	0	0	0

Dynamic parameters of the robotic arm-container assembly are shown in Tab. 3.
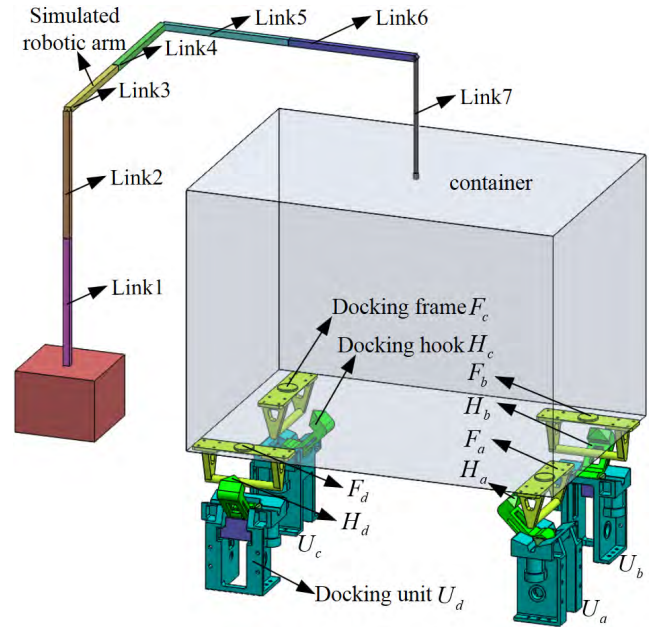

FIGURE 10. System model.

TABLE 3. Dynamic parameters of robotic arm-container assembly.

NO.	Mass /kg	Centroid vector /mm	Moment of inertia /kg · mm	Viscous damping /N/(m/s)
1	0.0548	[0,0,100]	[731.12,0.91,731.12]	0.1
2	0.0548	[0,-100,0]	[731.12,0.91,731.12]	0.1
3	0.0548	[0,0,100]	[731.12,0.91,731.12]	0.1
4	0.0548	[0,-100,0]	[731.12,0.91,731.12]	0.1
5	0.0548	[0,0,100]	[731.12,0.91,731.12]	0.1
6	0.0548	[0,-100,0]	[731.12,0.91,731.12]	0.1
7	71.192	[369.33,0,0]	[1.27e7,4.05 e6, 1.41 e7]	0.1

The docking mission is successful under the condition in which the docking hook tip passes through the rectangular docking frame. The length of the docking frame in the z direction increases and the height in the y direction decreases, as shown in Fig. 11. The main factor affecting the docking result during the docking process corresponds to the height of the docking frame. Therefore, key points are selected in the height direction for analysis. The midpoint of the upper border of the docking frame is denoted by A, the center of the locating shaft below is denoted by B, and C denotes the docking hook tip. To observe the docking process more intuitively, the three-dimensional structure is simplified as a two-dimensional figure. The docking component and position of each key point in Fig. 11, as viewed from the positive z-axis direction, are shown in Fig. 12(a).

With respect to the entire capture device shown in Fig. 10, the positions of the four capture frames simultaneously vary during the capture process, and should be observed simultaneously. The capture units U_a and U_c should be observed in
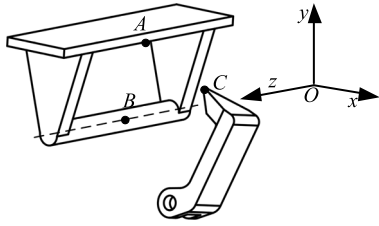
FIGURE 11. Key points of docking components.

(a) Positional relationship of docking unit U_c. (b) Positional relationship of docking unit U_b.

(c) Positional relationship of docking unit U_d. (d) Positional relationship of docking unit U_a.
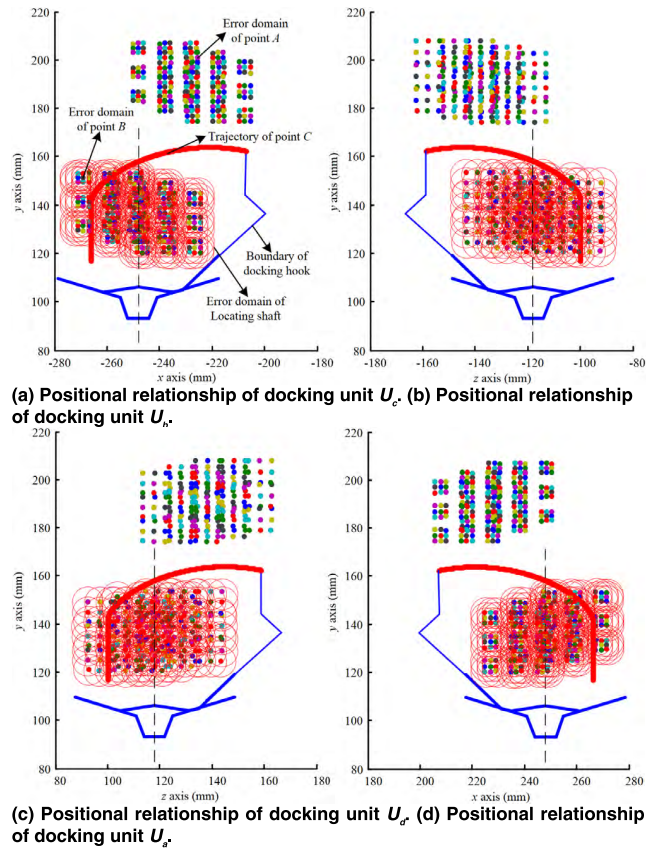
FIGURE 12. Positional relationship of the docking components corresponding to the limit pose set P_{Em}.

the main view, and the capture units U_b and U_d are observed in the left view. We consider the example of the limit error set E_0 corresponding to the tolerance domain T_0, and the error domain of the capture frame key points caused by the 64 limit errors is shown in Fig. 12. The layout of the positional relationship of the four capture units in Fig. 12 correspond to the layout of the capture units, as shown in Fig. 10.

The 64 limit poses are divided into four types. According to the symmetry characteristics of the orthogonal distributed docking device, we can only analyze 16 limit poses in the first type. The corresponding limit errors are shown in Tab. 4.

By observing the 16 limit errors in the first type, it was found that eight limit errors in the $-y$ axis direction are

TABLE 4. 16 limit poses in the first type.

NO.	x/mm	y/mm	z/mm	α /°	β /°	γ /°
1	-10	-10	-10	1	-1	-1
2	-10	-10	10	1	-1	-1
3	-10	10	-10	1	-1	-1
4	-10	10	10	1	-1	-1
5	10	-10	10	1	-1	-1
6	10	10	10	1	-1	-1
7	-10	-10	10	1	1	-1
8	-10	10	10	1	1	-1
9	-10	-10	-10	-1	-1	-1
10	-10	-10	10	-1	-1	-1
11	-10	10	-10	-1	-1	-1
12	-10	10	10	-1	-1	-1
13	10	-10	-10	-1	-1	-1
14	10	10	-10	-1	-1	-1
15	-10	-10	-10	-1	1	-1
16	-10	10	-10	-1	1	-1

-10 mm, and the other eight limit errors in the y axis direction are 10 mm. Because the $-y$ axis direction is the escape direction of the container, it is necessary to test the eight limit errors of 10 mm along the $+y$ axis direction. The limit errors corresponding to eight typical limit poses are shown in Tab. 5.

TABLE 5. Limit errors corresponding to eight typical limit poses.

No.	x/mm	y/mm (T_0)	y/mm (T)	z/mm	α /°	β /°	γ /°
1	-10	10	20	-10	1	-1	-1
2	-10	10	20	10	1	-1	-1
3	10	10	20	10	1	-1	-1
4	-10	10	20	10	1	1	-1
5	-10	10	20	-10	-1	-1	-1
6	-10	10	20	10	-1	-1	-1
7	10	10	20	-10	-1	-1	-1
8	-10	10	20	-10	-1	1	-1

The tolerance capacity can be obtained based on the docking determination of the eight typical limiting poses. Similarly, $T + \Delta T$ can be simplified in the same way. The analysis is carried out according to the tolerance capacity analysis method proposed in section II B. Owing to the size constraints of the structure, the tolerance can only be improved in the $-y$ axis direction, and thus let $\Delta T = [0mm, 1mm, 0mm, 0°, 0°, 0°]$. A continuous increase in T increases the corresponding eight limit errors, and the corresponding limit poses are judged for docking. Through the simulation and theoretical analysis, it was concluded that $n = 10$. The y axis direction tolerance capacity is increased by 50% from -10 to 20 mm, that is, the tolerance capacity reaches up to $T = [\pm10mm, -10 \sim 20mm, \pm10mm, \pm1°, \pm1°, \pm1°]$. The eight limit errors corresponding to the tolerance capacity T are shown in Table 5, and
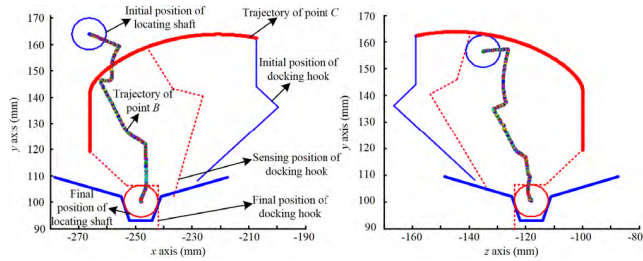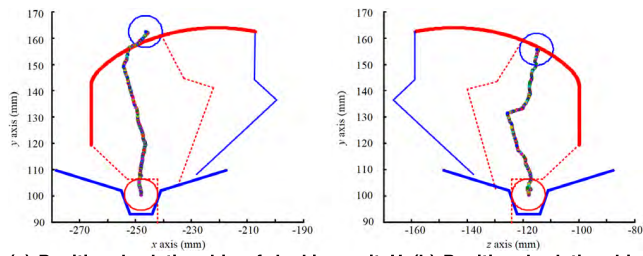
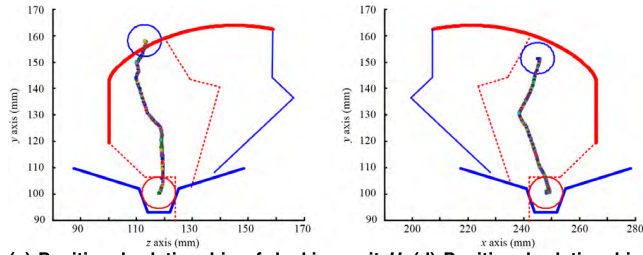(a) Positional relationship of docking unit U_c (b) Positional relationship of docking unit U_b
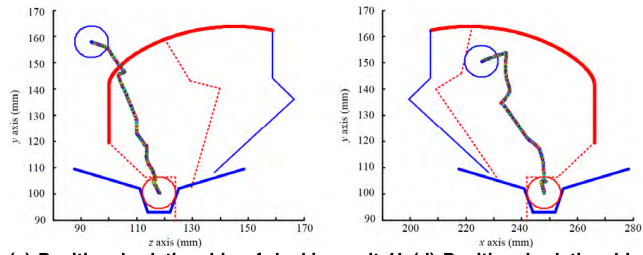
(c) Positional relationship of docking unit U_d (d) Positional relationship of docking unit U_a

FIGURE 13. Positional relation of docking components corresponding to the first limit pose.

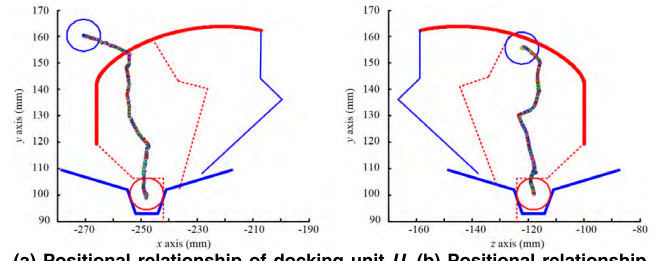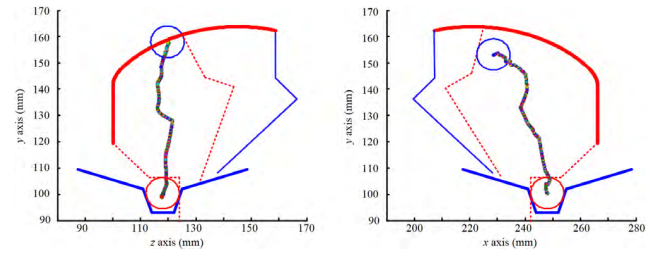(a) Positional relationship of docking unit U_c (b) Positional relationship of docking unit U_b

(c) Positional relationship of docking unit U_d (d) Positional relationship of docking unit U_a

FIGURE 15. Positional relation of docking components corresponding to the third limit pose.

(a) Positional relationship of docking unit U_c (b) Positional relationship of docking unit U_b

(c) Positional relationship of docking unit U_d (d) Positional relationship of docking unit U_a

FIGURE 14. Positional relation of docking components corresponding to the second limit pose.

(a) Positional relationship of docking unit U_c (b) Positional relationship of docking unit U_b

(c) Positional relationship of docking unit U_d (d) Positional relationship of docking unit U_a

FIGURE 16. Positional relation of docking components corresponding to the fourth limit pose.

the eight limit poses corresponding to the limit errors are all successfully docked during the docking simulation process. Owing to space limitations, only the first four limit poses were graphically expressed during the docking process, as shown in Figs. 13–16.

Observation of the trajectory of the corresponding docking components under the four limiting poses showed that the positions of the four positioning shafts continuously change, and finally enter the positioning groove of the docking unit
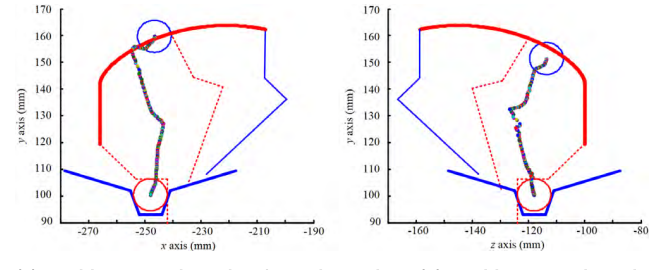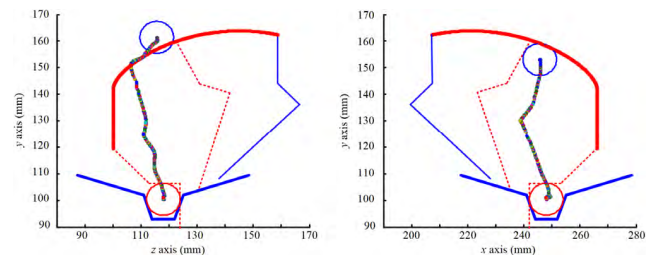
base, thereby indicating the successful docking of the docking device to the container. The docking of the device to the container under the eight limit poses was successful, and the tolerance capacity of the docking device achieved was $T = [\pm 10mm, -10mm \sim 20mm, \pm 10mm, \pm 1°, \pm 1°, \pm 1°]$.

V. EXPERIMENT
A. EXPERIMENT SYSTEM
In combination with the orthogonal distributed docking device described herein, a docking experiment system was

designed and developed. The docking experiment system is composed of a six degree-of-freedom (6-DoF) pose adjustment system, a 7-DoF simulation robotic arm, a 3-DoF matching centroid system, a simulated container, a 6-DoF force sensor, an orthogonal distributed docking device, and a control system, as shown in Fig. 17.
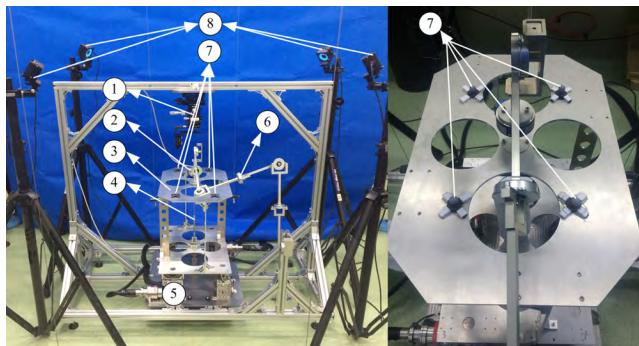
1. 6-DoF pose adjustment system 2. 6-DoF force sensor 3. Simulated container 4. 3-DoF matching centroid system 5. Orthogonal distributed docking device 6. 7-DoF simulation robotic arm 7. Target 8. Camera,

FIGURE 17. Docking experiment system.

The 6-DoF pose adjustment system is connected by three translation platforms and three rotating platforms in accordance with specific positional relations. After connecting with the container handle, the initial pose of the simulated container can be adjusted. The 7-DoF simulated robotic arm is composed of a simulated arm and a joint damper. During the docking process, the joint damper can generate damping proportional to the motion speed, effectively simulating the robotic arm in a zero-force control state during the actual docking process. The counterweight method is used to simulate the microgravity environment in space, and the suspension at the center of mass of the container can effectively simulate the floating state of the container in space. The 3-DoF counterweight aligning system can change the spatial position of the suspension point through an adjustment of the bolts. The centroid of the simulated container can be accurately found by adjusting the suspension point when errors occur during the processing and assembly of the simulated container. To reduce the counterweight load, a simulated lightweight container was developed. The envelope size of the simulated container is exactly the same as that of an actual container, although the quality is less than that of the actual container. The 6-DoF force sensor is installed at the end of the simulated robotic arm. When the docking hook comes into contact with the docking frame, the sensor will sense the force signal and feed it back to the control system, providing a basis for the selection of the control strategy.

During the adaptive docking experiment, the motion capture system is used to detect the pose of the container. It uses four cameras to monitor the positional changes of the four targets and obtain the motion trajectory of the centroid of the

simulated container. The camera layout and target positions are shown in Fig. 17.

After calibration of the four cameras used in the motion capture system and the overall coordinate system, the coordinates of the four targets can be monitored. Through the automatic transformation and a later calculation of the control software, the change in trajectory of the coordinates of the centroid of the container can be obtained. The target images received by the four cameras and the positions of the cameras in the control software are as shown in Fig. 18.
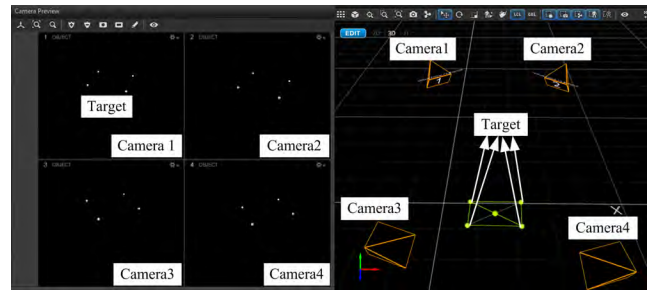

FIGURE 18. Target images and positions of four cameras.

B. FRACTIONAL-STEP ADAPTIVE DOCKING EXPERIMENT

The docking experiment platform and motion capture system were used for the adaptive docking experiment. The four limit poses analyzed in Section IV were adopted, along with the adaptive docking strategy applied in the corresponding docking approach described in section IV. The centroid displacement curves of the four sets of docking experiments as compared with simulation are shown in Figs. 19–22. CDE indicates the centroid displacement of the experiment, CDS is the centroid displacement of the simulation, and TFPCD is the theoretical final position of the centroid displacement.

It can be seen from the comparison of the centroid displacements obtained through the adaptive docking test and the simulation analysis that both the centroid displacement curves approach the theoretical final position of centroid displacement. In the first group of docking tests, the largest displacement error of the centroid is in the z direction, and the displacement error of the centroid relative to the simulation analysis is 1.8%. In the second group of docking tests, the largest displacement error of the centroid is in the z direction, and the displacement error of the centroid relative to the simulation analysis is 7.7%. In the third group of the docking tests, the largest displacement error of the centroid is in the y direction, and the displacement error of the centroid relative to the simulation analysis is 2.6%. In the fourth group of docking tests, the largest displacement error of the centroid is in the x direction, and the displacement error of the centroid relative to the simulation analysis is 9.3%. There are errors in the two curves because the simulation analysis is an ideal analysis process, and some error factors appear in the test verification, such as an error in the machining accuracy of the experiment system, a contact stiffness error, or a damping
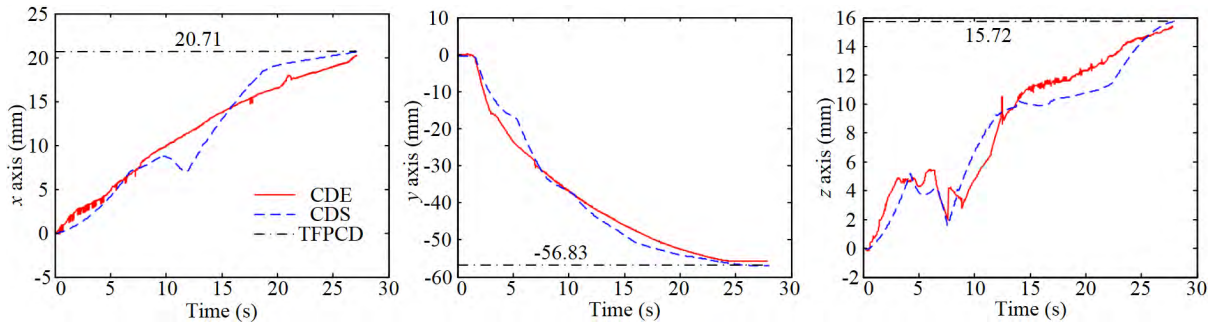
FIGURE 19. Centroid displacement curve of docking experiment compared with simulation for the first limit pose.
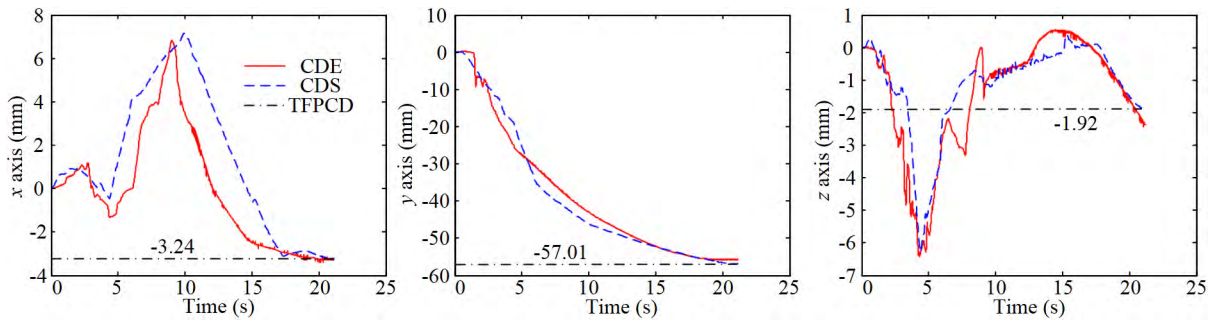

FIGURE 20. Centroid displacement curve of docking experiment compared with simulation for the second limit pose.
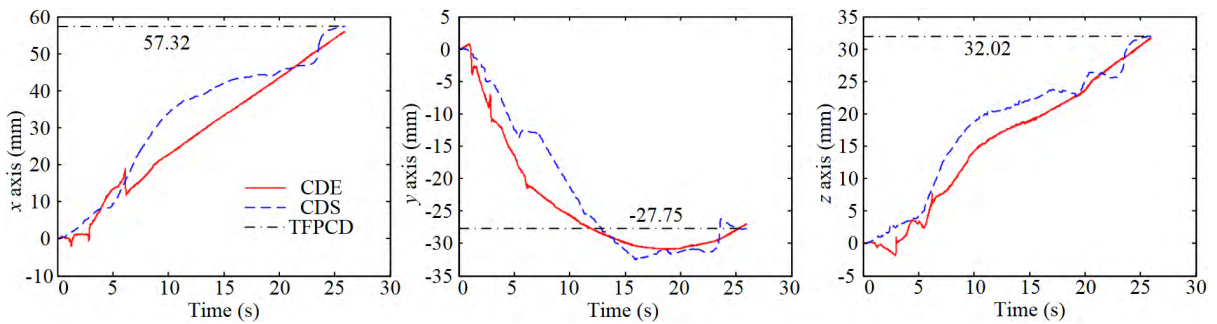

FIGURE 21. Centroid displacement curve of docking experiment compared with simulation for the third limit pose.
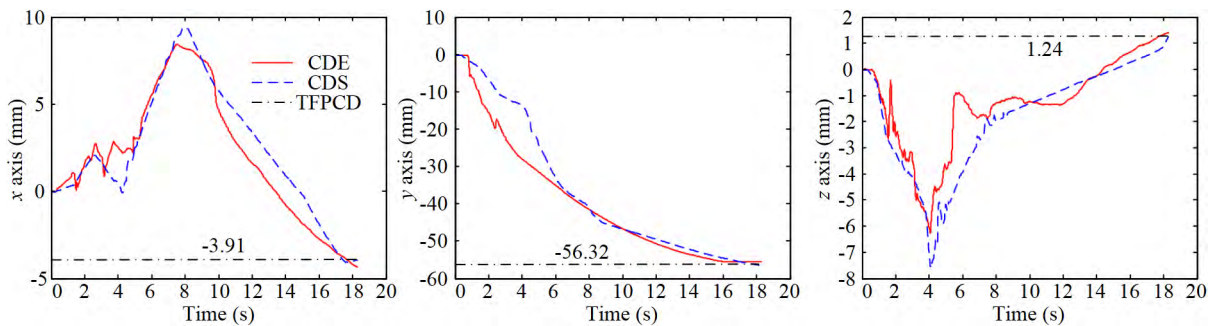

FIGURE 22. Centroid displacement curve of docking experiment compared with simulation for the fourth limit pose.

error in the simulated robotic arm joint. The change trends of the two curves during the docking process are the same, and the values are similar, which proves the correctness of the simulation analysis and the test verification, and proves the feasibility of the adaptive docking strategy in improving the level of tolerance.

VI. CONCLUSION

This paper described a study on a docking strategy for an orthogonally distributed docking device. The following conclusions were obtained:

(1) An adaptive docking strategy for an orthogonally distributed container docking device was proposed, which can significantly improve the tolerance of the docking device.

(2) The dynamic model of the orthogonally distributed docking device was established, and the tolerance capacity of the adaptive docking strategy was determined through a simulation analysis.

(3) A prototype of the orthogonally distributed docking device was developed, and a docking test platform was built. An experimental verification of the proposed adaptive docking strategy was carried out, and a comparison between the simulation analysis and the experiment verification proved the feasibility of the adaptive docking strategy in improving the tolerance capacity.

ACKNOWLEDGMENT

REFERENCES

[1] J. C. Martin and G. W. Law, "Suborbital reusable launch vehicles and applicable markets," Office Space Commercialization, United States Dept. Commerce, Washington, DC, USA, Tech. Rep. PB2003-102442, 2002, pp. 3–13.

[2] R. J. Gorski, "A space based orbital transfer vehicle operating from the space station," in *Proc. Space Station 21st Century*, 1986, p. 2325.

[3] G. Wang, F. Yang, S. Jiang, H. Yue, Y. Lu, and M. Wu, "Determination method of capture for an orthogonal distributed satellite capture device," *IEEE Access*, vol. 6, pp. 61800–61811, 2018.

[4] G. Wang, F. Yang, H. Yue, and S. Jiang, "Optimal layout method of distributed locking device of satellite based on plant root growth theory," *Proc. Inst. Mech. Eng. G, J. Aerosp. Eng.* , vol. 233, no. 8, pp. 2802–2818, 2019.

[5] B. S. Yu, D. P. Jin, and H. Wen, "Analytical deployment control law for a flexible tethered satellite system," *Aerosp. Sci. Technol.*, vol. 66, pp. 294–303, Jul. 2017.

[6] J. Virgili-Llop, J. V. Drew, R. Zappulla, II, and M. Romano, "Laboratory experiments of resident space object capture by a spacecraft–manipulator system," *Aerosp. Sci. Technol.*, vol. 71, pp. 530–545, Dec. 2017.

[7] Q. Li, J. Yuan, B. Zhang, and C. Gao, "Model predictive control for autonomous rendezvous and docking with a tumbling target," *Aerosp. Sci. Technol.*, vol. 69, pp. 700–711, Oct. 2017.

[8] Z. Su, and H. Wang, "Probe motion compound control for autonomous aerial refueling docking," *Aerosp. Sci. Technol.*, vol. 72, pp. 1–13, Jan. 2018.

[9] *Kibo Handbook*, Jpn. Aerosp. Explor. Agency (JAXA) Hum. Space Syst. Utilization Program Group, Tokyo, Japan, Sep. 2007.

[10] J. O'Sullivan, *Japanese Missions to the International Space Station*. Cham, Switzerland: Springer, 2019, pp. 91–130.

[11] M. Okasha, C. Park, and S.-Y. Park, "Guidance and control for satellite in-orbit-self-assembly proximity operations," *Aerosp. Sci. Technol.*, vol. 41, pp. 289–302, Feb. 2015.

[12] P. Motaghedi and S. Stamm, "6 DOF testing of the orbital express capture system (Invited Paper)," *Proc. SPIE*, vol. 5799, pp. 66–82, May 2005.

[13] E. Arnieri, L. Boccia, G. Di Massa, and G. Amendola, "A compact high gain antenna for small satellite applications," *IEEE Trans. Antennas Propag.*, vol. 55, no. 2, pp. 277–282, Feb. 2007.

[14] E. Papadopoulos and S. A. A. Moosavian, "Dynamics and control of multi-arm space robots during chase and capture operations," in *Proc. IEEE/RSJ/GI Int. Conf. Intell. Robots Syst., Adv. Robot. Syst. Real World (IROS)*, vol. 3, Sep. 1994, pp. 1554–1561.

[15] M. Oda, "Space robot experiments on NASDA's ETS-VII satellite-preliminary overview of the experiment results," in *Proc. IEEE Int. Conf. Robot. Automat.*, vol. 2, May 1999, pp. 1390–1395.

[16] B. A. Aikenhead, R. G. Daniell, and F. M. Davis, "Canadarm and the space shuttle," *J. Vac. Sci. Technol. A, Vac. Surf. Films*, vol. 1, no. 2, pp. 126–132, 1983.

[17] R. G. Daniell and S. S. Sachdev, "The design and development of an end effector for the shuttle remote manipulator system," NASA, Washington, DC, USA, Tech. Rep. N82-23344, 1982, pp. 45–62.

[18] E. Endo, H. Mitsuma, R. Sakata, T. Itoko, and Y. Taniguchi, "Berthing and docking mechanisms for future Japanese space structures," in *Proc. 28th Aerosp. Sci. Meeting*, Reno, NV, USA, 1990, p. 516.

[19] M. Hardt, C. Mas, D. Cocho, L. Mollinedo, O. Gracia, P. Urmston, and A. Ayuso, "Validation of space vehicle docking with the international berthing & docking mechanism and a Kuka robot," in *Proc. 14th Eur. Space Mech. Tribol. Symp.*, Konstanz, Germany. 2011, pp. 113–120.

[20] A. Tsuchihashi, N. Noguchi, and K. Kuraoka, "End effector," U.S. Patent 4 955 654, Sep. 11, 1990.

[21] J. Wang, R. Mukherji, M. Ficocelli, A. Ogilvie, M. Liu, and C. Rice, "Modeling and simulation of robotic system for servicing hubble space telescope," in *Proc. IEEE/RSJ Int. Conf. Intell. Robots Syst.*, Oct. 2006, pp. 1026–1031.

[22] J. Wang, R. Mukherji, M. Ficocelli, A. Ogilvie, and C. Rice, "Contact dynamics simulations for robotic servicing of the hubble space telescope," *Proc. SPIE*, vol. 6221, May 2006, Art. no. 622103.

[23] H. Liu, Y. Tan, Y. Liu, D. Jie, K. Gao, and H. G. Cai, "Development of Chinese large-scale space end-effector," *J. Central South Univ. Technol.*, vol. 18, no. 3, pp. 600–609, 2011.

[24] F. Feng, Y.-W. Liu, H. Liu, H.-G. Cai, "Development of space end-effector with capabilities of misalignment tolerance and soft docking based on tendon-sheath transmission system," *J. Central South Univ.*, vol. 20, no. 11, pp. 3015–3030, 2013.

[25] Y. Zhang, K. Sun, H. Liu, and Y. Zhang, "Pose measurement of nozzle based on laser range finders for capturing satellite," *Proc. Inst. Mech. Eng. G, J. Aerosp. Eng.*, vol. 230, no. 8, pp. 1385–1396, 2016.

[26] T. Yang, N. Sun, H. Chen, and Y. Fang, "Neural network-based adaptive antiswing control of an underactuated ship-mounted crane with roll motions and input dead zones," *IEEE Trans. Neural Netw. Learn. Syst.*, to be published.

[27] N. Sun, Y. Wu, H. Chen, and Y. Fang, "An energy-optimal solution for transportation control of cranes with double pendulum dynamics: Design and experiments," *Mech. Syst. Signal Process.*, vol. 102, pp. 87–101, Mar. 2018.

[28] G. Wang, Z. Xie, Y. Lu, J. Wang, M. Wu, F. Yang, H. Yue, and S. Jiang, "Analysis method of the capture tolerance capability for an orthogonally distributed satellite capture device," *IEEE Access*, vol. 7, pp. 55022–55034, 2019.
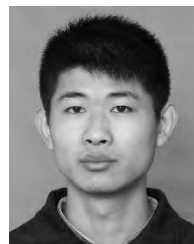
GANG WANG was born in Dezhou, Shandong, China, in 1989. He received the B.S. degree in mechanical design and theory from Shandong Jianzhu University, Jinan, in 2012, and the M.S. degree in aerospace science and technology from the Harbin Institute of Technology, Harbin, China, in 2015, where he is currently pursuing the Ph.D. degree in aerospace science and technology. He is mainly engaged in the research of space capture mechanism on orbit.

ZHIJIE XIE received the Ph.D. degree from the Harbin Institute of Technology (HIT), in 2014, where he is currently a Lecturer of aerospace science and technology. His research interests include the development of mechanical basic components and the research of space capture mechanism on orbit.

XINGKE MU received the B.S. and M.S. degrees in mechanical design and theory from Harbin Engineering University, Harbin, China, in 2007 and 2009, respectively. He is currently with the China Academy of Launch Vehicle Technology. He was promoted to Senior Engineer, in 2018. His main research interest includes the spacecraft mechanism designs.

SHAOZHEN LI was born in Jiaozuo, Henan, China, in 1994. He received the B.S. degree in aerocraft manufacture engineering from the Harbin Institute of Technology, Harbin, China, in 2017, where he is currently pursuing the M.S. degree in aerospace science and technology. He is mainly engaged in the research of magnetic levitation system used for isolation.

FEI YANG was born in Yuncheng, Shanxi, China, in 1985. He received the B.S. degree in mechanical design and theory from Guizhou University, Guiyang, in 2007, and the M.S. and Ph.D. degrees in mechanical design and theory from the Harbin Institute of Technology, Harbin, China, in 2014, where he was a Research Assistant, from 2014 to 2017. He was promoted to Associate Professor, in 2017. He is mainly involved in research on wheeled planetary vehicle mobility and space capture.

HONGHAO YUE was born in 1978. He is currently a Professor and Ph.D. Candidate Supervisor with the Research Center of Aerospace Mechanism Control, Harbin Institute of Technology, China. He has published more than 40 academic papers in international famous periodicals and important international academic conferences and one English publication. He holds four national invention patents. His main research interests include mechatronics engineering and active vibration control of smart structures. He received various awards, such as two national technological inventions, two first prizes of Heilongjiang's technological invention, and two awards of science and technology progress of the whole army.

SHENGYUAN JIANG received the Ph.D. degree in mechanical design and theory from the Harbin Institute of Technology, Harbin, China, in 2001. Since 2002, he has been with Beihua University, Jilin, China, where he is currently a Professor with the School of Mechanical Engineering. In 2007, he was elected as a Grantee of the New Century Excellent Talent Subsidizing Scheme from the Education Ministry. He has authored or coauthored more than 40 papers and has been granted three Chinese patents of invention. His research interests include pipeline robotics, mechatronics, and virtual prototype technology.

● ● ●